

A FEASIBILITY STUDY ON THE BEHAVIOUR OF A HELICOPTER SMART BLADE AIMED AT BLADE TIP MORPHING

CLAUDIO TESTA

INSEAN – Italian Ship Model Basin, Propulsion and Cavitation Department, Rome, Italy
e-mail: c.testa@insean.it

STEFANIA LEONE

University of Palermo, Transport Engineering Department, Palermo, Italy
e-mail: leone@diat.unipa.it

SALVATORE AMEDURI

ANTONIO CONCILIO

CIRA - Italian Aerospace Research Center, Smart Structures Laboratory, Capua, Italy
e-mail: s.ameduri@cira.it; a.concilio@cira.it

In this paper, the behaviour of a hingeless helicopter blade with a novel integrated smart morphing actuator is studied. The proposed smart device is aimed at the reduction of BVI noise through transformation of the blade tip shape into an anhedral tip type and is based on the concept of a variable-stiffness blade. In detail, the blade morphing is obtained through joint action of a magneto-rheological-fluid (MRF) device, shape-memory alloy (SMA) tie-rods and a set of concentrated masses properly distributed spanwise. In this architecture, the MRF system has to provide local bending-stiffness reduction and concentrated masses have to provide inertial moments whereas the SMA tie-rods have to mould the blade tip shape. Since the equilibrium configuration of the smart blade deeply depends on the interaction between the aeroelastic response and the actuation loads, in this work a numerical investigation examines potentiality and shortcomings of the proposed integrated smart system to morph a realistic blade with respect to the baseline configuration.

Key words: smart structures, anhedral helicopter blade

List of symbols

- ν – lag displacement
- w – flap displacement
- Φ – angle of torsion
- μ – mass per unit length

Ω	–	rotational speed
EI_z, EI_y	–	bending stiffness (in plane and out of plane, respectively)
ϑ	–	blade pre-twist
GJ	–	torsional stiffness
x	–	spanwise position
R	–	radius of blade
β_{pc}	–	precone angle
e_A	–	tension axis offset from elastic axis
k_{m1}, k_{m2}	–	principal mass radius of gyration
k_A	–	blade cross-section polar radius
L_v, L_w	–	sectional aerodynamic load (in plane and out of plane, respectively)
M_ϕ	–	sectional aerodynamic torsional moment
F_w^{act}	–	actuation force
M_ϕ^{act}	–	actuation moment
t	–	thickness of blade cross section
m_k	–	k -th concentrated mass
ρ	–	air density
cl_α	–	airfoil lift curve slope
v_i	–	local induced velocity
e_d	–	chordwise offset of aerodynamic centre behind elastic axis
σ	–	blade solidity
N_b	–	number of blade
L	–	annular valve depth
h	–	difference between external and internal valve circumferences
T_{MR}	–	contribution to shear stress on valve lateral walls due to fluid activation
R_p	–	piston base radius.

1. Introduction

Since the first half of the 90's the rotorcraft community has devoted considerable efforts towards the enhancement of helicopter performances by integrating smart systems into main rotor blades. Blade morphing is one of the techniques that may be applied to this aim even if the extremely complex environment related to rotating blades affects the capability of it. In fact, high energy levels and significant displacements, forces, moments involved, make unpractical some engineering solutions based on smart materials integrated into the rotor system that, in principle, are expected to guarantee light-weight and adapti-

vity. Thus, in spite of the availability of different strategies based on current technologies involved in the reduction of noise and vibration, their practical realisation is currently limited to few approaches. The evaluation of noise generated by rotating blades is one of the most important analysis related to the helicopter main rotor performance and acoustic certification. The smart architecture examined here is devoted to reduction of aerodynamically generated noise in low-speed descent flight (and sometimes in hovering or fly-over conditions). In this operating condition, the acoustic annoyance is mainly due to the blade-vortex interaction phenomenon (BVI). It occurs when strong tip vortices, dominating the rotor wake, impinge or pass closely to the rotor blades resulting in impulsive changes of the blade loads that produce, in turn, high noise and vibration levels. It is well documented (Johnson, 1980) that the interaction of the shed tip vortex with the following blade induces vibrations, increases pilot workload and reduces component fatigue life increasing maintenance costs. A possible strategy to alleviate the BVI noise is to diffuse the blade tip vortex or displace it far away from the following blades by increasing the blade vortex miss-distance. Such a solution may be achieved through an anhedral tip shape. Previous research (Prouty, 1993; Tung and Lee, 1994) has shown that typically the *tip* vortex involved in the blade-vortex impinging is related to a spanwise length of about 10-15% of the blade radius from the tip (controlled zone) and noise is reduced if a mean slope variation of 5° , at least, is achieved.

The authors faced the problem of transforming the blade tip region into an anhedral shape in the past (Testa *et al.*, 2005) referring to a simplified structural model and coming to an elementary smart actuation system without inertial effects. Taking advantage from that work, in this paper, an innovative integrated smart stiffness-variable system is examined and a feasibility study is addressed to investigate its potentiality. The basic concept is to achieve the desired blade morphing by exploiting the energy of the centrifugal field in addition to actions provided by actuators based on piezoelectric materials (PZT), shape memory alloys (SMA), etc. To this purpose, a magneto-rheological device, located within the controlled zone, has to allow local spanwise reduction of the bending stiffness (against the centrifugal stiffening) when switched-on, whereas the action of SMA elements combined to bending moments induced by eccentric masses (properly distributed inside the blade box) have to bend the rotating blade to obtain an anhedral configuration. In the following, the numerical study is addressed to test the feasibility of the proposed smart concept for helicopters; the evaluation of BVI noise and its reduction is, therefore, beyond the aim of this work and is postponed to further studies.

2. Actuation strategy

The smart system proposed in this work is based on a quite new way of thinking in the framework of actuation systems for rotating blades. Indeed, it combines the advantages of an adaptive stiffness beam with the energy developed by the rotating environment when eccentric masses are properly located into the blade box. In detail, the capability to morph the blade tip is based on an *on/off* system composed of a magneto-rheological fluid-based device (MRF), a shape memory alloy-based device (SMA) and a set of concentrated masses properly distributed inside the blade box. The MRF system provides a spanwise local control of the bending stiffness, whereas the SMA tie-rod actuator, combined with the forces induced by the eccentric masses, bends the structure. When no anhedral configuration is needed, a magnetic field is applied to the MRF device so that the fluid viscosity increases and the blade controlled zone is completely locked. In this case, the SMA tie-rod is switched-off and the masses are still located in their rest position on the elastic axis. On the contrary, when the anhedral shape is needed (i.e. descent flight or hovering) the magnetic field is decreased thus reducing the bending stiffness and the concentrated masses are suitably displaced above the elastic axis and the SMA elements are switched-on. In such a way, the joint bending action of the concentrated masses and SMA actuator deflects the blade tip region. Once the required anhedral shape is achieved, the SMA actuator is switched-off and the magnetic field is increased until the equilibrium configuration is frozen.

Figures 1a and 1b show a sketch of the blade and the lay-out of the smart system, respectively. In Fig. 1c a zoom of the controlled zone is shown.

3. An aeroelastic model of the smart blade

The evaluation of the performance of the proposed smart architecture in terms of capability to change the blade shape, needs modelling of the coupling between the aeroelastic loads and actuation forces. Thus, in the following, a physically consistent aeroelastic model, including all the actions induced by the actuators embedded into the elastic structure, is briefly outlined. The descent flight condition should be studied; however, in order to derive some guidelines on the behaviour of the smart blade, the attention is focused on the hover condition. The aeroelastic formulation used in this work is obtained by coupling the equations of the blade dynamics introduced in Hodges and Dowell

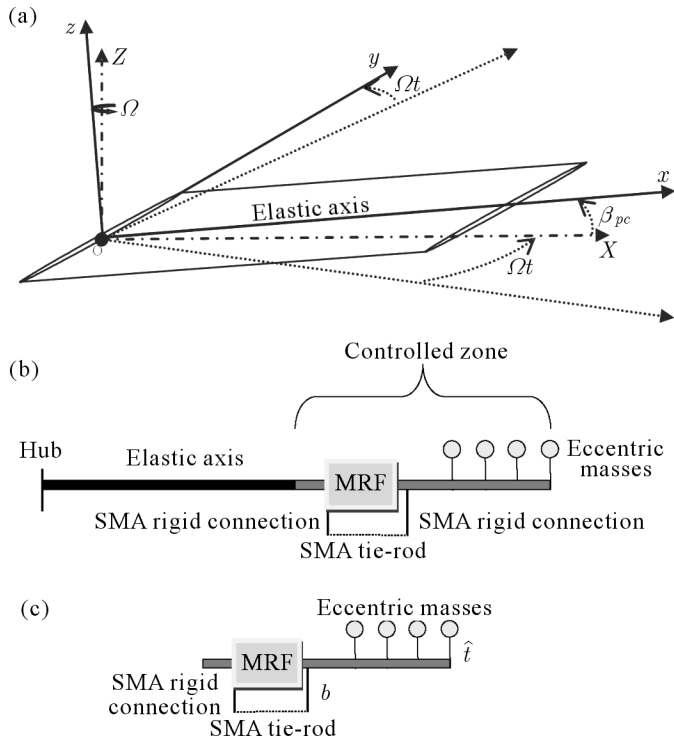


Fig. 1. (a) 3D blade; (b) lay-out of the integrated smart system; (c) zoom of the controlled zone

(1974) with the aerodynamic loads given by a quasi-steady 2D theory based on the Greenberg theory (Hodges and Ormiston, 1976). Although the aerodynamic model is quite simple, it is commonly used by helicopter industries for evaluating the blade response at very low frequency analysis. To take into account the 3D trailing vortices effect, the wake-inflow correction is included. This model is an extension of the formulation used in Testa *et al.* (2005), where only the flapping motion is considered. The hingeless rotor blade is modelled as a long, straight, slender, homogeneous isotropic beam; the theory is intended for moderate displacements, accurate to the second order, and based on the hypothesis that squares of the bending slopes, twist, thickness-radius and chord-radius ratios are small with respect to unity. Radial non-uniformities (mass, stiffness, twist, etc.), chordwise offsets of the mass centroid and tension axes from the elastic axis, pre-cone and warping are included; other details, such as blade root feathering flexibility, torque offset, blade sweep and droop are not herein considered. Thus, by assuming that the blade is inextensible

for bending deformations and neglecting the radial displacement, the blade aeroelastic model may be written as

$$\begin{aligned}
 & -\left[v' \int_x^R \mu \Omega^2 x \, dx\right]' - \mu \Omega^2 [v + e \cos(\vartheta + \phi)] - \left[(e - e_A) \mu \Omega^2 x \cos(\vartheta + \phi)\right]' + \\
 & + \left\{ [EI_z - (EI_z - EI_y) \sin^2(\vartheta + \phi)] v'' + \frac{1}{2} (EI_z - EI_y) \sin 2(\vartheta + \phi) w'' \right\}'' = L_v \\
 & -\left[w' \int_x^R \mu \Omega^2 x \, dx\right]' - [(e - e_A) \mu \Omega^2 x \sin(\vartheta + \phi)]' + \mu \Omega^2 \beta_{pc} x + \\
 & + \left\{ [EI_y - (EI_z - EI_y) \sin^2(\vartheta + \phi)] w'' + \frac{1}{2} (EI_z - EI_y) \sin 2(\vartheta + \phi) v'' \right\}'' = \\
 & = L_w + F_w^{act} \tag{3.1} \\
 & -k_A^2 \Omega^2 \left[(\phi + \vartheta)' \int_x^R \mu x \, dx \right]' + \mu \Omega^2 \phi (k_{m2}^2 - k_{m1}^2) \cos 2\vartheta + \\
 & + (EI_z - EI_y) \left[v'' w'' \cos 2\vartheta + \frac{1}{2} (w''^2 - v''^2) \sin 2\vartheta \right] + \\
 & + \mu e \Omega^2 x (w' \cos \vartheta - v' \sin \vartheta) - (GJ\phi')' - e_A (w'' \cos \vartheta - v'' \sin \vartheta) \left[\int_x^R \mu \Omega^2 x \, dx \right] + \\
 & + \mu \Omega^2 (k_{m2}^2 - k_{m1}^2) \cos \vartheta \sin \vartheta + \mu e \Omega^2 \beta_{pc} x \cos \vartheta = M_\phi + M_\phi^{act}
 \end{aligned}$$

where the unknowns are the in-plane (lead-lag, $v(x)$) and the out-of-plane (flap, $w(x)$) displacements of the elastic axis, as well as the cross-section torsion $\phi(x)$ around it. The bending and torsional stiffness are represented by EI_y , EI_z and GJ , respectively, μ is the blade mass for unit length and x the spanwise position. In addition, k_{m1} and k_{m2} are the principal mass radii of gyration, k_A is the blade cross-section polar radius of gyration, β_{pc} – pre-cone angle, e – centre of mass offset from the elastic axis and e_A – tension axis offset from the elastic axis. The blade pre-twist is assumed to be linear and expressed as

$$\vartheta = \vartheta_{75} + \vartheta_{tw} \left(\frac{x}{R} - \frac{3}{4} \right) \tag{3.2}$$

where ϑ_{75} is the blade pitch at 75% span (including collective pitch) and ϑ_{tw} is the blade linear pre-twist.

The forcing terms at the right-hand side of equation (3.1) are the sum of the sectional aerodynamic loads (L_v , L_w , M_ϕ) and the loads given by the actuation device (F_w^{act} and M_ϕ^{act}). From the description of the smart system

given in Section 2, the actuation loads come from localized bending moments exerted by the action of eccentric masses and SMA tie-rods and read (no lagwise action loads arises)

$$\begin{aligned}
 F_w^{act} &= \Omega^2 \hat{t} \sum_k [m_k \delta'(x - x_k) x_k] - F_{sma} b [\delta'(x - x_c) - \delta'(x - x_d)] \\
 M_\phi^{act} &= \Omega^2 \hat{t} \sum_k [m_k \delta(x - x_k) x_k v'_k] - F_{sma} b [\delta(x - x_c) v'_c - \delta(x - x_d) v'_d]
 \end{aligned}
 \tag{3.3}$$

In equations (3.3), m_k is the k -th concentrated mass located at the abscissa x_k on the elastic axis, \hat{t} denotes a portion of the cross-section thickness, v'_k is the lag-bending slope at x_k , F_{sma} is the axial force provided by the SMA actuator, b is the arm with respect to the beam axis, Ω is the rotor angular velocity and $\delta(x)$ the Dirac delta function. Concerning the aerodynamic loads, the lagwise section load L_v , the flapwise section load L_w , and the sectional pitching moment about the elastic centre M_ϕ , for a steady-state hovering configuration are given by Hodges and Ormiston (1976)

$$\begin{aligned}
 L_v &= \frac{\rho_\infty c l_\alpha c}{2} \left[v_i^2 - \Omega^2 x^2 \frac{c d_0}{c l_\alpha} - \Omega x v_i (\vartheta + \phi) \right] \\
 L_w &= \frac{\rho_\infty c l_\alpha c}{2} \cdot \\
 &\quad \cdot \left[-\Omega x v_i + \Omega^2 x^2 (\vartheta + \phi + \int_0^x v' w'' dx) + \Omega^2 \frac{x c}{2} (\beta_{pc} + w') - \Omega^2 x v (\beta_{pc} + w') \right] \\
 M_\phi &= M_{ac} + e_d L_w
 \end{aligned}
 \tag{3.4}$$

where ρ denotes air density, c is the local chord, $c l_\alpha$ – airfoil lift curve slope, e_d – chordwise offset of the aerodynamic centre behind the elastic axis and v_i – local induced velocity. The wake behind the rotor disk determines the induced inflow distribution over the disk and plays an important role in the prediction of the aeroelastic behaviour of the main rotor. Hence, accurate modelling of the wake is important for rotor analysis, more so at low flight speed where the wake stays close to the disk and deeply affects the blade airloads. There are many wake models available with varying levels of complexity and accuracy. In this work, the inflow velocity is supposed steady, uniform along the span and equal to the value of non-uniform inflow given by the blade element momentum theory (BEMT) (Hodges and Ormiston, 1976) at the radial station $0.75R$

$$v_i = \text{sgn}(\vartheta + \phi_{75}) \Omega R \frac{\pi \sigma}{8} \left(\sqrt{1 + \frac{12}{\pi \sigma} |\vartheta + \phi_{75}|} - 1 \right)
 \tag{3.5}$$

where $\sigma = N_b c / (\pi R)$ is the blade solidity and ϕ_{75} indicates the elastic twist at the radial station $0.75R$.

As shown in Section 5, the use of the idealized uniform inflow induces rotor behaviour fairly different from that predicted by the blade element momentum theory: the comparative analysis therein performed highlights that the uniform inflow model increases the blade aeroelastic displacements. Although the uniform inflow seems to be too coarse with respect to the simple, but more realistic, BEMT model, it allows one to investigate the aeroelastic response of the integrated smart blade in more severe aeroelastic conditions where major bending and torsional loads act. From a numerical standpoint, it allows conservative analysis of the smart rotor. A further refinement of the inflow calculation requires consideration of details of the rotor vortex wake; however, at the beginning of this feasibility study the use of simple and widely used engineering numerical tools seems to be a good choice with respect to the required accuracy.

4. Steady equilibrium configuration

The finite element method (FEM) is used for integration of equations (3.1) that yields the equilibrium configuration of the smart blade. To this aim, the blade is divided into N beam-elements, having three nodes (two boundary and an interior one) and 11 degrees of freedom. Each boundary node, of any element, is characterized by 5 DOFs (v, v', w, w', ϕ), while the internal one is used for taking into account the elastic twist only. Hence, for lag and flap bending deflections, the interpolating polynomial is chosen from the family of Hermite's polynomials, while Lagrangian polynomials are used for the elastic twist.

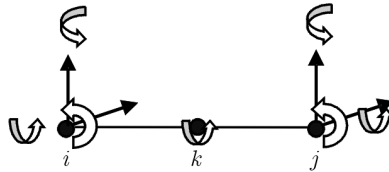


Fig. 2. Nodal forces and moments

For the i -th beam element, the introduction of the matrix shape functions yields the local field displacement as

$$\mathbf{u}^e(x) = \mathbf{H}(x)\mathbf{q}^e \quad (4.1)$$

where the matrix shape functions and the nodal displacements are respectively given by

$$\mathbf{H}(x) = \begin{bmatrix} \mathbf{N}(x) & \mathbf{0} & \mathbf{0} \\ \mathbf{0} & \mathbf{N}(x) & \mathbf{0} \\ \mathbf{0} & \mathbf{0} & \mathbf{N}_\phi(x) \end{bmatrix} \quad (4.2)$$

$$\mathbf{q}^{e\top} = [v_i, v'_i, v_j, v'_j, w_i, w'_i, w_j, w'_j, \phi_i, \phi_k, \phi_j]$$

with \mathbf{N} , \mathbf{N}_ϕ being the sub-matrices containing the interpolating polynomials for bending and torsional displacements, respectively. Finally, the application of the FE method transforms equations (3.1) into the following discretized form

$$\mathbf{K}\boldsymbol{\delta} = \mathbf{F}_0 + \mathbf{F}_{NL}(\boldsymbol{\delta}) \quad (4.3)$$

where $\boldsymbol{\delta}$ denotes the vector collecting the degrees of freedom of all elements. At the left-hand side, the global aeroelastic stiffness-matrix \mathbf{K} is derived from the linear contribution of aerodynamics and structural loads, including the centrifugal stiffening, whereas the global nodal-loads \mathbf{F}_0 and \mathbf{F}_{NL} , at the right-hand side, account for the constant and non-linear terms from the structure, aerodynamics and actuation. The solution to equation (4.3) is obtained iteratively through application of the Newton-Raphson method that, at the k -th iteration, yields

$$\left(\mathbf{K} - \frac{\partial \mathbf{F}_{NL}}{\partial \boldsymbol{\delta}} \Big|_k \right) \boldsymbol{\delta}^{k+1} = \mathbf{Q}_0 - \frac{\partial \mathbf{F}_{NL}}{\partial \boldsymbol{\delta}} \Big|_k \boldsymbol{\delta}^k \quad (4.4)$$

Note that the blade equilibrium configuration must satisfy the propulsive trim equation in hovering, that is, the vehicle weight W must be balanced by the rotor thrust T : the elastic displacements and the collective angle corresponding to the equilibrium conditions are determined jointly by solving equation (4.4) coupled with the trim equation $T - W = 0$.

5. Numerical results

Before showing the results concerning the smart blade, some numerical findings are shown to validate the methodology of Section 4 through which steady responses are obtained.

To this aim, the untwisted cantilever beam considered in Kwon (1988) has been examined. It has a uniform mass and stiffness distribution, no offsets

between elastic, mass, tension and aerodynamic axes. Figures 3a, 3b and 3c illustrate the equilibrium tip deflections (flap, lag and torsion) at different precone angles and demonstrate that the agreement with the solution given in Kwon (1988) is very good.

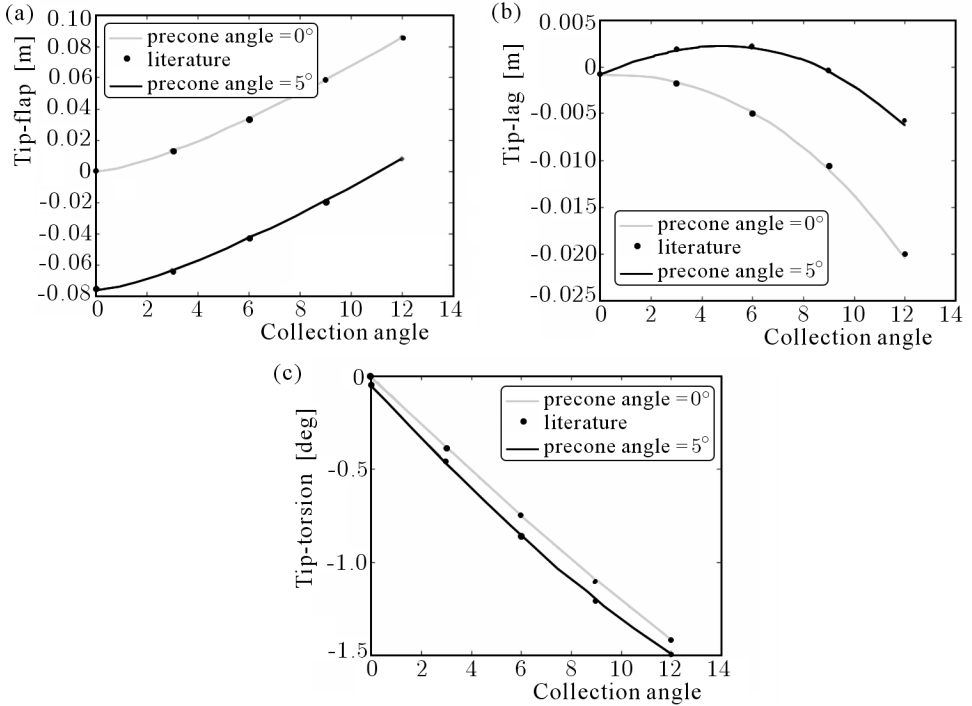


Fig. 3. Equilibrium blade tip deflections

For the same blade configuration, Fig. 4 shows the spanwise distribution of the induced velocity due to the blade element momentum theory, after the steady equilibrium state is reached. The assumption of a steady uniform induced velocity distribution along the span predicts too high downwash at the blade root sections and a too low value in the outer portion of the blade.

Coherently, Fig. 5 shows that the aerodynamic load L_w associated with the constant induced velocity modelling is lower at the blade root sections and higher in the outer portion of the blade span. The resulting flapwise displacements are shown in Fig. 6: the presence of constant downwash induced velocity causes greater flap displacements.

For the sake of completeness, lag and torsion displacements are shown in Figs. 7a and 7b, respectively.

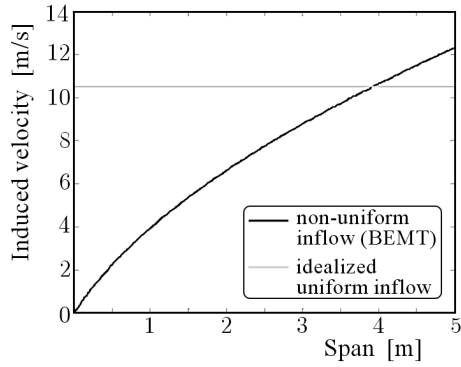


Fig. 4. Spanwise distribution of the induced velocity

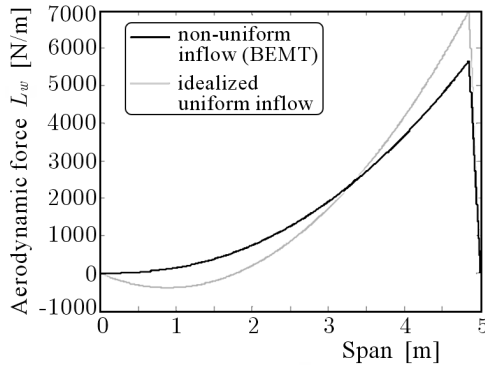


Fig. 5. Spanwise distribution of flapwise load

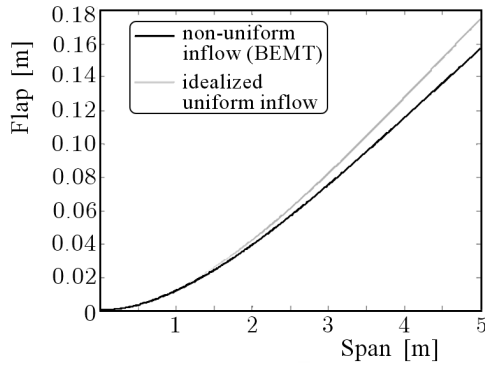


Fig. 6. Flap displacements

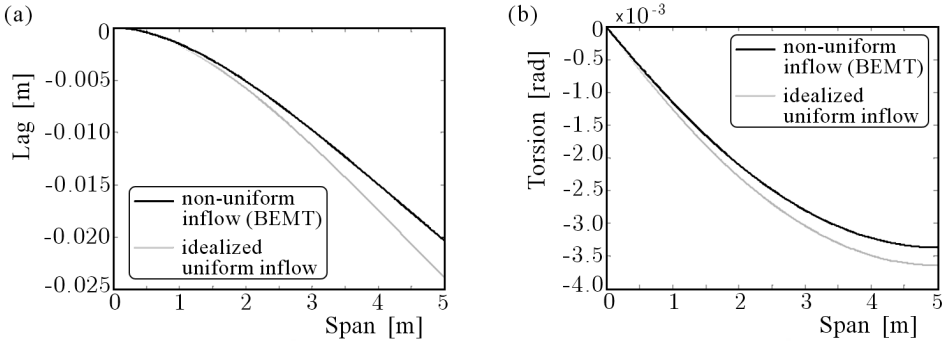


Fig. 7. (a) Lag displacements; (b) torsion

Next we discuss the application of the smart morphing device; its capability to change the shape of the blade tip is investigated through a numerical study performed on a Bo105-type four-bladed rotor having a NACA 0015 cross-section, radius $R = 4.9$ m, local chord $c = 0.27$ m, precone angle $\beta_{pc} = 2.5^\circ$ and a rotational speed $\Omega = 44$ rad/s (Spletstoesser *et al.*, 1993). This analysis is aimed at presenting potentialities and drawbacks of the smart device and to clarify the reason why the coupled action of more devices (MRF, SMA and eccentric masses) is necessary to achieve an anhedral shape. Therefore, in the following, the effect induced by the three devices, is studied separately.

5.1. Effect of the MRF device

The presence of the MRF system is modelled only within the controlled zone (15% tip blade portion). In particular, a preliminary parametric study (not shown here) indicates that a higher morphing effect of the controlled zone implies a spanwise stiffness reduction localized between $0.87R$ and $0.9R$, corresponding to 13% and 10% of the blade span (starting from the tip), respectively. On the basis of this choice, different bending-stiffness reductions are simulated and the related blade equilibrium configurations are evaluated.

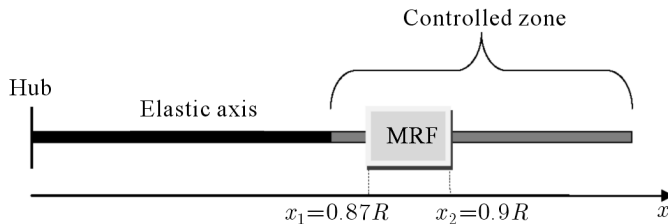


Fig. 8. Sketch of the elastic axis with the integrated MFR device

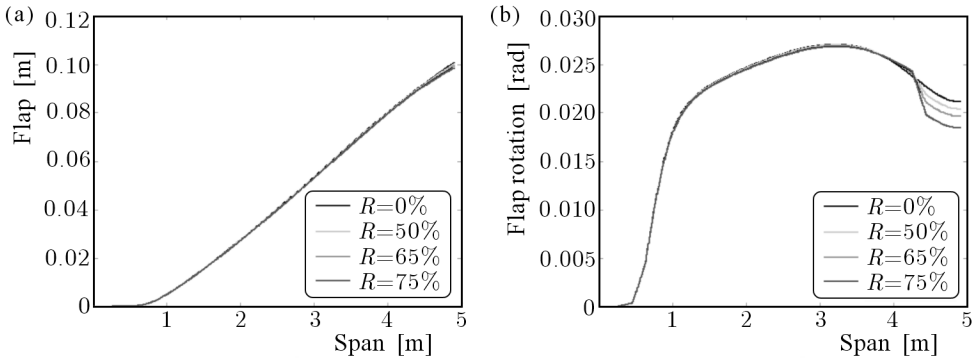


Fig. 9. (a) Out-of-plane displacement; (b) flap rotation

As shown in Fig. 9, the blade shape remains very close to the non-actuated one even for a stiffness reduction \mathfrak{R} equal to 65% of the initial stiffness. However, by defining a bending slope variation index, conventionally, as $\Delta\vartheta = w'_{tip} - w'_2$ (w'_2 is the flap-bending slope at x_2), it results that for $\mathfrak{R} = 75\%$ of the initial stiffness a slope variation $\Delta\vartheta = -0.002$ rad is achieved. The comparison between the non-activated and the activated blade shows that the flap tip displacement remains quite unchanged, $w_{tip} \cong 0.1$ m, whereas $\Delta\vartheta$ is slightly increased from -0.0017 rad to -0.002 rad. In order to preserve the necessary robustness, that is, to avoid transforming the controlled zone into a real hinged-beam and experiencing too large displacements, the weakening provided by the MRF device cannot be too large. This is the reason why no further stiffness reductions are considered. Note that the structural stiffness reduction acts in a small region near the blade tip; thus, only slight variations of the natural rotating frequencies appear, as shown in Fig. 10, where the first six frequencies are plotted.

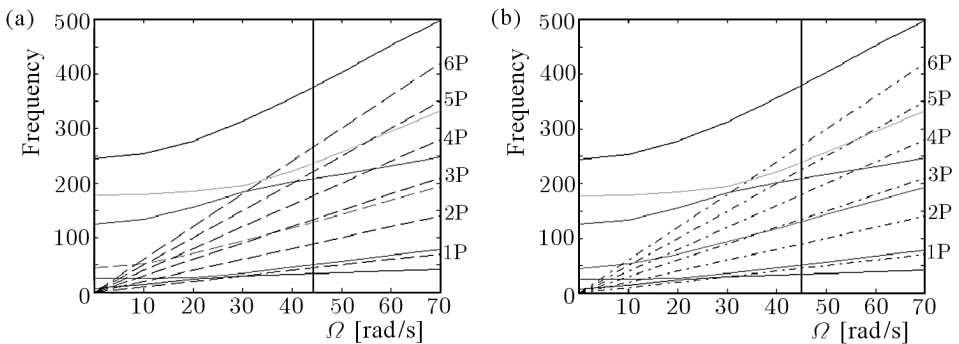


Fig. 10. Fan diagram: (a) non-activated blade; (b) weakened blade by MRF

As a matter of fact, the actuation of the MRF device produces only a slight variation of the blade tip shape.

5.2. Effect of the SMA-based device

A preliminary investigation has been performed to obtain the spanwise position of the SMA actuator; the outcome of this parametric study was that, for an efficient use of the SMA device in terms of induced-bending effects, it has to be positioned between $0.87R$ and $0.92R$, corresponding to 13% and 8% of the blade span (starting from the tip), respectively (see Fig. 11). For this configuration, the length b of the rigid connection results in the 6% of the local chord ($b = 0.0162$ m).

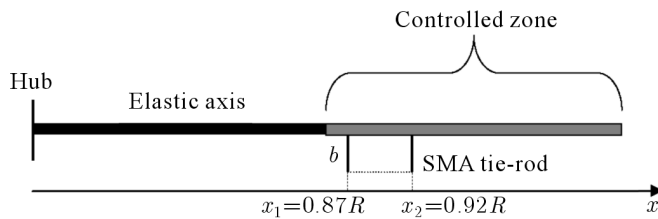


Fig. 11. Sketch of the elastic axis with the integrated SMA actuator

The investigation on the effects due only to the SMA actuator reveals that the corresponding flap bending moments modify somehow the structure (see Fig. 12). As expected, the best configuration is achieved when the maximum allowable number of ribbons (computed with reference to the internal space) is used. For the blade considered in Splettstoesser *et al.* (1993), 30 the ribbons, providing a 15 kN force, produce a slope variation $\Delta\vartheta = -0.0042$ rad and a tip displacement $w_{tip} = 0.0982$ m. Hence, the activation of the SMA actuator produces a greater slope variation than the MRF device.

5.3. Effect of the MRF and SMA devices

Coupling the SMA actuator with the MRF device enhances the advantages of local stiffness reduction. However, in this case, the weakening provided by the MRF cannot be too large because of the coupling between the aeroelastic forces and actuator actions. In particular, numerical investigations show that for a realistic four-bladed rotor, \mathfrak{R} has to be not greater than 50% of the initial stiffness. Limiting \mathfrak{R} to 50% of the initial stiffness, the combined action of MRF and SMA yields $\Delta\vartheta = -0.0046$ rad and $w_{tip} = 0.096$ m (see Fig. 13).

A shortcoming of this actuation strategy is that the blade morphing is achieved when SMA and MRF devices run at the maximum of their own ca-

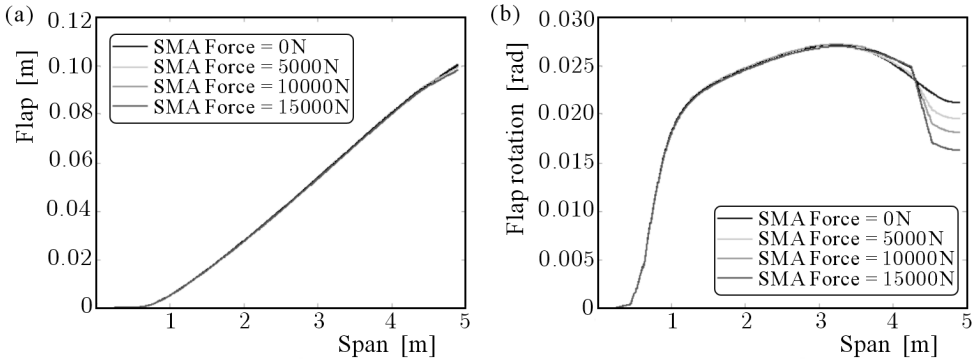


Fig. 12. Effect of the SMA actuator: (a) flap displacement; (b) rotation

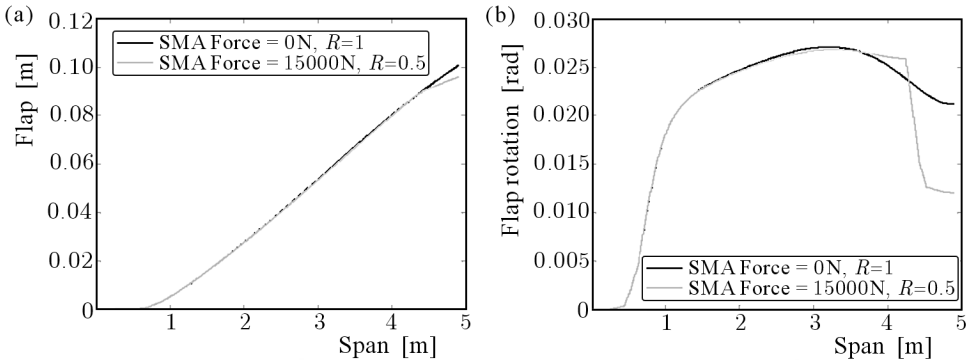


Fig. 13. Effect of the SMA/ MRF-based actuation: (a) flap displacement; (b) rotation

pability. This problem may be overcome by incorporating the actions induced by the centrifugal field. Before showing this important result, it is convenient, for the sake of clarity, to summarize the previous investigations. To this purpose, Fig. 14 depicts the effects induced by the different actuation strategies.

5.4. Inclusion of eccentric masses

The smart configuration herein proposed is composed of the MRF and SMA devices with the inclusion of eccentric masses properly located inside the blade box above the elastic axis.

A preliminary investigation aimed at assessing the *best* lay-out of the smart architecture integrated into the blade has been performed and the outcome of it was that the SMA actuator has to be positioned between $0.87R$ and $0.92R$, the MRF device between $0.87R$ and $0.9R$ and at least three masses (properly

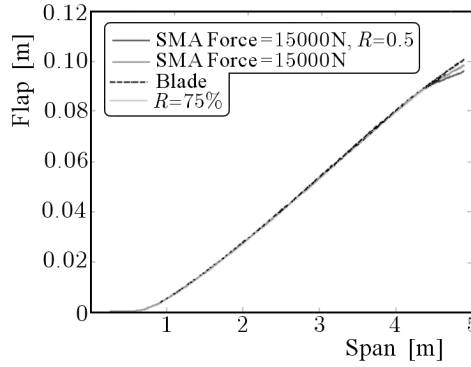


Fig. 14. Comparison among different actuation strategies

located spanwise and of suitable amount) are required to achieve the anhedral shape. Making reference to Fig. 15, two concentrated masses m_1 , m_2 , located just beyond the MRF-SMA device towards the tip and a mass M , placed at the blade tip, are considered. It results that m_1 is located at $0.93R$ whereas m_2 is located at $0.97R$.

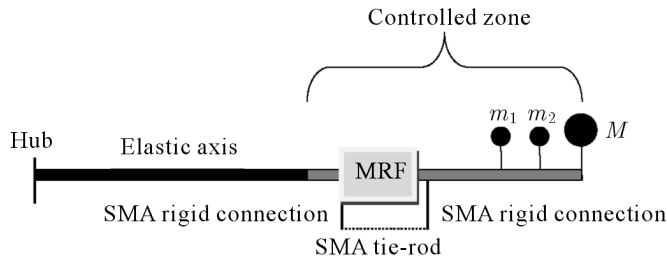


Fig. 15. Sketch of the investigated architecture

The mass m_1 is aimed at improving the effect of the MRF-SMA system, m_2 at allowing the moulding of the blade shape, whereas M at modifying the blade shape for achieving the anhedral configuration.

It is worth noting that in the MRF-SMA-based actuation system examined in Section 5.3, the shape memory alloys are called to bend the outer portion of the blade while through the use of concentrated masses, the centrifugal field is devoted to yield the major bending effect with the SMA actuator used to provide a local change in the bending slope in the area where the MRF device acts (so that the characteristic *beak profile* is obtained).

In details, the numerical analysis shows that by using $m_1 = m_2 = 0.25$ kg, $M = 1.5$ kg (corresponding to the mass increase that is equal to 8% of the blade mass), $\mathfrak{R} = 50\%$ to the initial stiffness, $\hat{t} = b = 0.0162$ m and using

15 SMA ribbons, the bending slope variation obtained is $\Delta\vartheta = -0.01645$ rad with a tip deflection $w_{tip} = 0.076$ m (see Fig. 16). Note that in this case, the difference between the bending slope at 10% of the span (from the tip) on the basic blade and the slope at the blade tip of the actuated blade yields a bending slope variation equal to -2.2° , which corresponds to 44% of the requirement (bending slope variation equals to -5° , see Prouty (1993), Tung and Lee (1994)).

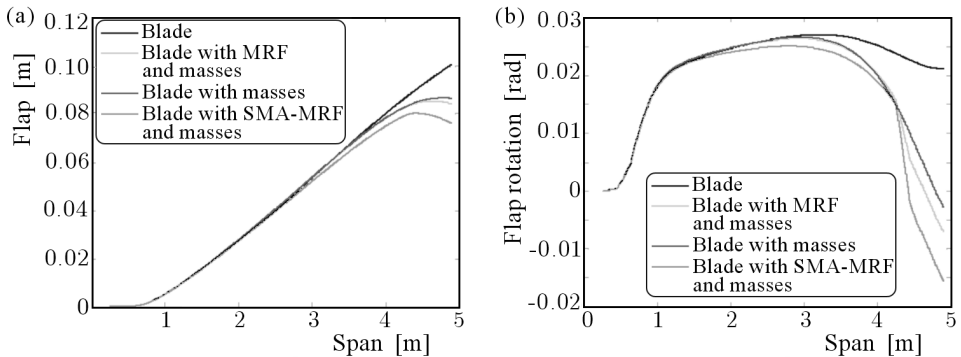


Fig. 16. Effect of the concentrated masses: (a) flap displacement; (b) rotation

Anyway, the satisfaction of the requirement is well beyond the scope of this investigation because the purpose of the present work is to address a feasibility study on a realistic helicopter main rotor in order to analyse the capabilities of the proposed integrated smart system and derive useful preliminary guidelines on the rotorcraft blade morphing. Figure 16 depicts the comparison among different actuation strategies; starting from the basic blade (line 1) the inclusion of the three masses allow to obtain a different configuration (line 2). The use of a MRF device allows modifying that deformed shape (line 3). The inclusion of a SMA actuator allows one to reach the characteristic *beak profile* (line 4), with a tip vertical displacement slightly less than 0.08 m. This result could be improved, for instance, by increasing the amount of concentrated masses. However, the presence of eccentric masses must not lead to resonance values next to the rotor harmonics; operatively, any intersection between the rotating blade frequencies and the *n-per-rev* frequencies (nP) should be avoided within the characteristic rotor operating range. For instance, assuming a 15% global mass increase as the maximum allowed, the solution characterised by a 2 kg increase appears as a good compromise between the need of achieving the desiderate *beak* beam-shape and keeping away undesired resonances within the operating range. In fact, the blade under investigation has a nominal resonance at 40 rad/s, when $5P$ intersects the 2nd lag frequency (Fig. 10a); by

augmenting the global mass by 2 kg, this resonance occurs at 50 rad/s when $4P$ intersects the 2nd lag frequency (Fig. 17a). By increasing the added mass up to 4 kg, the undesired resonance at the nominal speed (44 rad/s) occurs (see Fig. 17b).

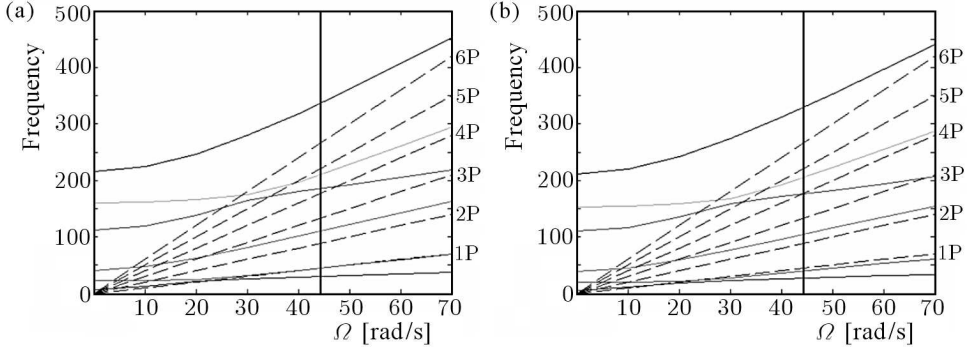


Fig. 17. Fan diagram: (a) 8% mass increase; (b) 15% mass increase

From this numerical investigation it results that the proposed smart system integrated into a realistic helicopter blade may be, in principle, effective in morphing the blade tip region so as to get an anhedral shape. However, the goal of blade morphing has to be matched both with the aimed BVI noise abatement and with the requirements concerning the rotor dynamic response. This implies that the amount of additional mass, bending-stiffness reduction and SMA wires strength have to be the result of a compromise between the need of amplifying the bending effect of the centrifugal field and the need of avoiding blade resonances for all flight conditions experienced by the helicopter. Other issues, concerning pitch control effectiveness in forward flight (when blade morphing is not needed) and aeroelastic stability of the non-actuated and actuated rotor affect the final design of the smart blade and should be considered; however they are beyond the aim of the paper.

6. Actuation power

In order to estimate the energy supplied to the SMA-MRF system, a numerical study is here addressed. The crucial point is the identification of the working condition of the devices. To this aim commercial devices whose properties are provided by the manufacturer, are considered.

6.1. MRF device

The MRF device considered in this section (Figs. 18 and 19) is composed of two cylinder-piston systems, connected by a wire to the upper and lower part of the virtual hinge. Because of the centrifugal field, to avoid separation of metal particles of the fluid, the magnetic device should be integrated close to the root (around 0.2m far from the rotation axis). In fact in this region, the centrifugal acceleration is estimated to be about 40 g, coherent with the maximum value of 80 g.

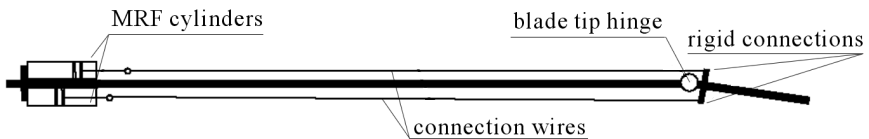


Fig. 18. Sketch of the MRF device

As shown in Fig. 19, each piston base splits the cylinder volume in two parts, filled by the magneto-rheological fluid. A hole allows the fluid to pass through and the piston to slide. If a suitable magnetic field is applied in this passage, fluid viscosity increases up to produce the piston lock; as a consequence, hinge freezing is produced through a wire element connecting the stem to the hinge (see Fig. 18).

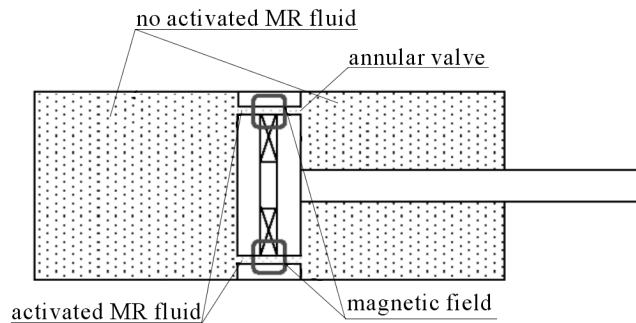


Fig. 19. MRF cylinder-piston main features

An important aspect concerning the MRF design is the evaluation of the maximum reaction force that the activated fluid is able to provide (locking force). From Srinivasan and McFarland (2001) it results that the maximum allowable pressure ΔP_p is given by

$$\Delta P_p = 2\tau_{MR} \frac{L}{h} \quad (6.1)$$

where L is the annular valve depth, h – difference between external and internal valve circumferences and τ_{MR} – contribution to the shear stress on the valve lateral walls due to fluid activation. Once the locking force is known, the above expression yields the minimum value of τ_{MR} that the applied magnetic field must provide. Previous numerical results for the fully-actuated blade show that the bending-stiffness reduction produced by the MRF has to be not greater than 50% of the initial stiffness. In order to evaluate the locking force, an iterative procedure may be conveniently used: trial forces to re-establish the equilibrium configuration of the baseline (non-weakened) blade are applied at the top of the rigid connections. For the structure under investigation, it results that 3 Nm moment, corresponding to the locking force equal to 185 N, is needed. For the sake of safety, the working condition is here performed using a higher locking force value (300 N). Making reference to a realistic MRF device with internal radius $R_i = 0.01$ m, piston base radius $R_p = 0.01$ m, annular valve depth $L = 0.1$ m and considering a difference between the external and internal valve circumferences equal to $h = 0.001$ m, Eq. (6.1) yields $\tau_{MR} \cong 1$ kPa. A devoted finite element (FE) analysis, performed by FEMMTM code, yields an evaluation of the *average* value of the magnetic inductance in the regions of interest that, in turn, allow the evaluation of the required current intensity through the use of specific *inductance-shear* characteristics for the selected magneto-rheological fluid (released by the manufacturer). For the 132 AD magneto-rheological fluid and by considering a device composed of three coils of one hundred copper wire turns, such analysis yields current intensity equal to 1 A, voltage drop equal to 0.4 V and power supply of 0.4 W (note that the piston axial symmetry allows one to model half device only, see Fig. 20a). The corresponding magnetic field is depicted in Fig. 20b and 20c.

6.2. SMA actuator

The tie-rod device is aimed at moulding the curvature of 10 % blade span extremity. To maximise the bending-stiffness reduction given by the MRF system, the SMA actuator is properly located between $0.87R$ and $0.92R$.

From Section 5.4, it results that 15 ribbons, providing 7 kN force in the fully-actuated configuration, are used. For the application under consideration, it is reasonable to assume an activation time not greater than twenty seconds. Within the limits of this assumption, a numerical investigation is addressed to predict the working condition of the actuator (working temperature and

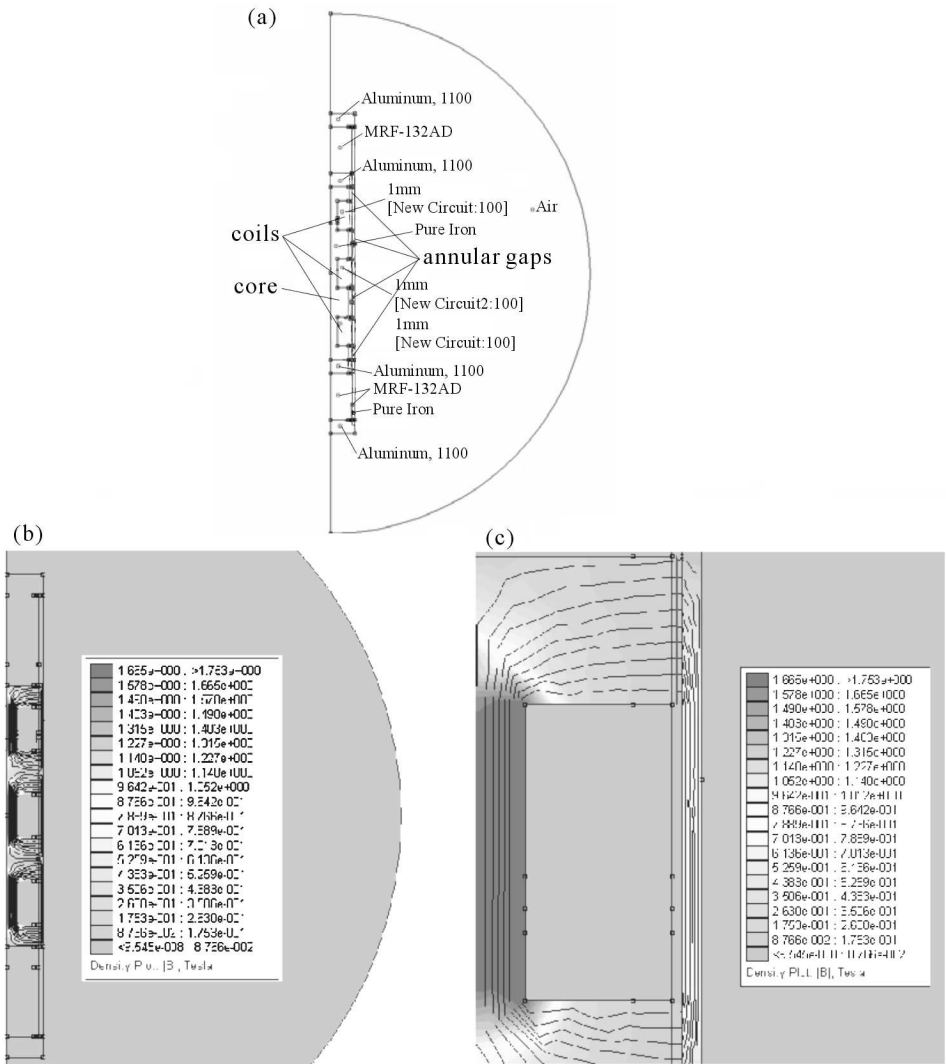


Fig. 20. FEMM™ FE model of the cylinder piston: (a) magnetic field distribution; (b) magnetic field detail in the gap zone; (c) zoom of the gap zone

wires recovery strain). To this aim, the aeroelastic model of the smart blade and SMA modelling (Liang and Rogers, 1990) are used jointly. Referring to a NiTiCu (10%) SMA wire (see Table 1), trial force values (within the range of 7 KN) are applied to the rigid connections of the fully-actuated blade (see Fig. 1b) to simulate the SMA bending effect and, in turn, to evaluate the resulting foreshortening of the wire element (Fig. 21, black curve). The SMA

working condition is then evaluated through the knowledge of the *SMA force vs. strain curves* for different temperatures (Liang and Rogers, 1990) (Fig. 21, grey curves). The outcome of this analysis is shown in Fig. 21, yielding the SMA operating temperature equal to 72.6°C and recovered strain equal to 0.2%. In these operating conditions, a power of about 30 W is required for the activation of a single SMA wire (having a length of 0.53 m) within a period of 20 s (see Ameduri and Gianvito, 2008). Hence, for the whole SMA device, 225 W must be supplied for each blade.

Table 1. Main features of the SMA actuator

Material	NiTiCu (10%)
Cross-section area	10 mm^2
Elements number	15
Length	0.25 m
Austenite activation temperatures: A_s , A_f	30°C , 60°C
Max recovery strain	3.0%
Martensite, austenite Young's moduli	20 GPa, 50 GPa
Resistivity (average value)	$200\ \mu\Omega/\text{cm}$

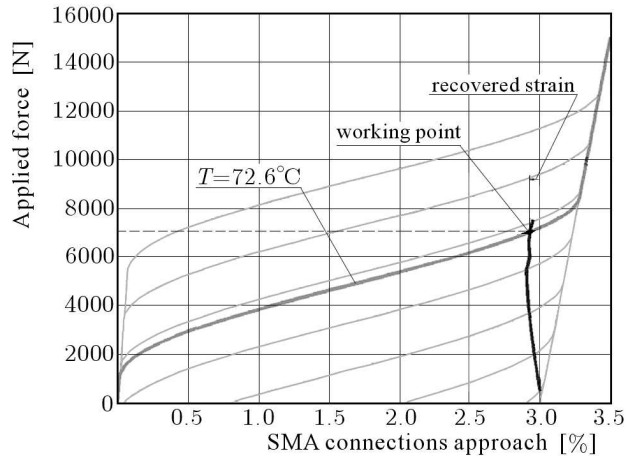


Fig. 21. SMA force – strain curves

7. Conclusions

In this paper, a feasibility study on the behaviour of a smart blade aimed at changing the shape of the blade tip region has been numerically investigated. The motivation of this study comes from the fact that the practical application of *on/off* devices integrated into rotating blades and aimed at blade morphing, is nowadays deeply limited by the actuation power involved. Hence, in spite of the need of achieving an anhedral shape in some flight conditions, the lack of suitable actuators make some engineering solutions typically used for reducing noise and vibration unpractical. For these reasons, the paper deals with a novel strategy of actuation based on the bending effect induced by the centrifugal field. To this purpose, the proposed actuator consists of concentrated masses properly located within the controlled zone (10-15% of the tip blade portion) and of suitable amount. To improve the bending action provided by this set of masses, a MRF device designed to decrease the bending-stiffness of the controlled zone, is considered. Finally, in order to mould the blade shape and increase the blade vortex miss-distance, a classical SMA-based actuator is analysed too.

Numerical results performed on a realistic Bo-105 type main rotor in hovering show the need of using the joint action of the three devices to achieve the anhedral shape. In particular, the spanwise location of the MRF device, SMA actuator and added masses as well as the number of SMA elements and the maximum allowable stiffness reduction are the result of a compromise between the need of amplifying the bending effect of the centrifugal field and SMA actuator and the need of assuring aeromechanical behaviour of the main rotor without resonances and aeroelastic instabilities for all flight conditions experienced by the helicopter.

Obviously, for a different blade type, the whole smart system should be re-designed. Hence, a tailored design should involve the design of the smart blade as a whole. At the same time, a devoted aeroacoustic study should be performed to evaluate the benefits in terms of noise reduction.

In conclusion, the results carried out from this numerical work are preliminary guidelines for rotorcraft blade morphing.

References

1. AMEDURI S., GIANVITO A., 2008, *Risultati Campagna Sperimentale di Caratterizzazione del Filo di SMA*, CIRA-CF-08-1198, Internal report, Capua (CE), September 2008 [in English]

2. HODGES D.H., DOWELL E.H., 1974, *Nonlinear Equation for the Elastic Bending and Torsion of Twisted nonuniform Rotor Blades*, NASA TND 7818
3. HODGES D.H., ORMISTON R., 1976, *Stability of Elastic Bending and Torsion of Uniform Cantilever Rotor Blades in Hover with Variable Structural Coupling*, NASA TND 8192
4. JOHNSON W., 1980, *Helicopter Theory*, Princeton University Press
5. KWON O.J., 1988, *A Technique for the Prediction of Aerodynamics and Aeroelasticity of Rotor Blades*, Phd Thesis, Georgia Institute of Technology
6. LIANG C., ROGERS C.A., 1990, One-dimensional thermomechanical constitutive relations for shape memory materials, *Journal of Intelligent Material Systems and Structures*, **1**, 207-233
7. PROUTY R.W., 1993, *Even More Helicopter Aerodynamics*, Chapter 29, Phillips Pub. Co.
8. SPLETTSTOESSER W.R, NIESL G., CENEDESE F., PAPANIKAS D.G., 1993, Experimental results of the European HELINOISE aeroacoustic rotor test in the DNW, *19th European Rotorcraft Forum Proceedings (Paper B8)*, Cernobbio, Italy
9. SRINIVASAN A.V., MCFARLAND D.M., 2001, *Smart Structures – Analysis and Design*, Cambridge University Press, pp. 73-96
10. TESTA C., LEONE S., AMEDURI S., CONCILIO A., 2005, Feasibility study on rotorcraft blade morphing in hovering, *12th SPIE International Symposium on Smart Structures and Materials (SPIE 2005)*, San Diego-California (USA)
11. TUNG C., LEE S., 1994, Evaluation of hover prediction codes, *Proceedings of the 50th Annual Forum of Am. Hel. Soc.*, Washington, DC

Studium wykonalności działania „ineligentnej” łopaty helikoptera wyposażonej w układ sterowania kształtem jej końca

Streszczenie

W pracy przedstawiono analizę właściwości bezprzegubowej łopaty helikoptera, w której zastosowano nowy, zintegrowany i aktywny układ oddziaływania na kształt łopaty. Zadaniem tego układu jest redukcja hałasu generowanego wskutek interakcji łopaty i wywołanych jej ruchem wirów ośrodka (*blade-vortex interaction* – BVI) poprzez zmianę kształtu końca łopaty celującego w uzyskanie ujemnego wzniosu. Metoda wykorzystuje koncepcję łopaty o zmiennej sztywności. W szczególności, kształtowanie łopaty jest sumarycznym efektem działania magneto-reologicznego aktuatora

(MRF), drążków wykonanych ze stopu z pamięcią kształtu (SMA) i zestawu mas skupionych odpowiednio rozłożonych wzdłuż łopaty. W takiej architekturze, podzespół MRF wprowadza lokalną redukcję sztywności giętnej, masy skupione wprowadzają dodatkowy moment bezwładności, podczas gdy drążki SMA sterują kształtem końca łopaty. Ponieważ konfiguracja położenia równowagi „inteligentnej” łopaty silnie zależy od aerosprężystej odpowiedzi układu oraz sił generowanych przez elementy wykonawcze (aktuatory), w pracy skupiono badania na numerycznej symulacji potencjału i ograniczeń wynikających z zastosowania zaproponowanej metody oddziaływania na kształt rzeczywistej łopaty względem konfiguracji bazowej.

Manuscript received November 7, 2008; accepted for print March 25, 2009